Thermal Science and Engineering Progress 65 (2025) 103888

Contents lists available at ScienceDirect

Thermal Science and Engineering Progress

journal homepage: www.elsevier.com/locate/tsep

Numerical investigations of the effects of gliding arc discharge on C_3H_8/air ignition using a new three-dimensional phenomenological model

Zhenyang Li [a,1], Ningqiu Zhao [b,2], Xiaochi Ma [b,2], Bo Yin [b,2], Qifu Lin [a,*], Yifei Zhu [b,**], Yun Wu [b,c,2], Yiman Jiang [d,3]

[a] Institute of Energy, Hefei Comprehensive National Science Center (Anhui Energy Laboratory), Hefei, 230088, China
[b] National Key Lab of Aerospace Power System and Plasma Technology, Xi'an Jiaotong University, Xi'an, 710049, China
[c] National Key Lab of Aerospace Power System and Plasma Technology, Air Force Engineering University, Xi'an, 710038, China
[d] Institute of Plasma Physics, Hefei Institute of Matter Science, Chinese Academy of Sciences, Hefei, 230031, China

ARTICLE INFO

Keywords:
Plasma-assisted combustion
Gliding arc discharge
Three-dimensional model
Kinetic effect
Propane

ABSTRACT

Ignition performance in extreme operating conditions limit performance improvements of aerospace engines. Plasma has attracted increasing attention due to its significant potential in improving ignition and combustion performance. This work presents the results of three-dimensional modeling of the effects of gliding arc (GA) discharge on C_3H_8/air ignition. A three-dimensional phenomenological gliding arc plasma-assisted ignition model is proposed considering the thermal and kinetic effects of plasma-assisted combustion. Two reduced plasma-assisted combustion mechanisms are proposed to investigate the role of $O(^1D)$ in GA-assisted combustion. The model is well validated against the nanosecond pulsed discharge in the evolution of O, $N_2(B)$, $N_2(C)$, and the gas temperature after vibrational–translational (V–T) relaxation. Additionally, the model has been validated against outlet temperature measurements with good agreement within the 300-600 W power range, and can simulate the GA-assisted ignition process with an ignition time uncertainty of 1.6%. The ignition process of C_3H_8 assisted by a 1100 W air GA is simulated. The results show that the GA discharge generates a significant amount of O and $O(^1D)$. The formation and consumption of O and $O(^1D)$ in GA discharge are firstly demonstrated: O atoms are primarily produced through the thermal dissociation reactions $O_2 + O \rightarrow O + O + O$ and $O_2 + N \rightarrow O + NO$, while $O(^1D)$ is mainly generated through the reactions $O_2(b^1\Sigma_g^+) + O \rightarrow O_2 + O(^1D)$ and the electron collision reaction $e + O \rightarrow e + O(^1D)$. The production of $O(^1D)$ depends on the O atoms generated through thermal dissociation reactions. At a power of 1100 W and a core GA temperature of 5000 K, $O(^1D)$ does not have a significant effect on the GA ignition process. This research advanced the understanding of ignition enhancement and key excited species by GA discharge, providing critical insights for optimizing combustor performance.

1. Introduction

The combustion chamber is a core component of an aero-engine. A combustor with a high stability and high-temperature rise can greatly increase the thrust-to-weight ratio for military aerospace engines [1]. As flight altitude increases and the stability of combustion decrease, a relatively wide lean blow-out (LBO) boundary and high-temperature rise are required for the engine combustor. Reductions in fuel consumption and pollutant emissions are major goals due to economic and environmental considerations for civil aviation engines [2]. So the combustors require high combustion efficiency and low pollutant emissions. Currently, high-altitude LBO and ignition or re-lighting in extreme operating conditions severely limit performance improvements of aerospace engines [3–5]. Plasma, recognized as the fourth state of matter, enhances combustion through three pathways: thermal, kinetic, and transport, establishing it as an advanced method for ignition and combustion enhancement.

The gliding arc (GA), possessing both thermal and non-thermal characteristics [6], is an ideal form of plasma-assisted ignition at an engineering scale. In recent years, numerous scholars have dedicated

* Correspondence to: No.80, Three Kingdoms City Road, Hefei, Anhui, China.
** Correspondence to: No.28 Xianning West Road, Xi'an, Shaanxi, China.
E-mail addresses: linqifu@ie.ah.cn (Q. Lin), yifei.zhu.plasma@gmail.com (Y. Zhu).
[1] No.80, Three Kingdoms City Road, Hefei, Anhui, China.
[2] No.28 Xianning West Road, Xi'an, Shaanxi, China.
[3] No.350 Shushanhu Road, Hefei, Anhui, China.

https://doi.org/10.1016/j.tsep.2025.103888
Received 26 March 2025; Received in revised form 15 July 2025; Accepted 17 July 2025
Available online 5 August 2025

Nomenclature

α, β	Stoichiometric coefficients of species A and B
η	Heat efficiency of the gliding arc
γ	Intermittency factor
κ	Volume fraction of the fine scale
μ	Electron mobility
μ_t	Turbulent viscosity coefficient
ν	Kinematic viscosity
ω	Gliding arc rotational angular velocity
ω	Reynolds-averaged momentum thickness Reynolds number
ϕ	Tilt angle of the gliding arc
ρ	Gas density
σ_k, σ_ω, σ_γ	Inverse effective Prandtl numbers for k, ω, γ
τ	Stress tensor
τ^*	Integrated timescale
θ	Angular coordinate
$\tilde{R}e_{\theta t}$	Specific dissipation rate
$\vec{g}$	Acceleration due to gravity
$\vec{V}$	Velocity vector
ξ^*	Length scale
a, b	Lengths of the minor and major axis
C_ξ	Length scale constant with a value of 2.1377
d	Length of the gliding arc
D_k, D_ω, and D_γ	Destruction terms for the respective quantities
E	Electric field intensity
E	Total energy
e	Elementary charge
h_i	Enthalpy of species i
I	Experimental current
J_i	Diffusion flux of species i
k	Turbulent kinetic energy
k_j	Reaction rate coefficient
k_{eff}	Effective thermal conductivity
L_{arc}	Gliding arc length
n_e	Electron density
p	Pressure
P_k, P_ω, P_γ, $P_{\theta t}$	Production terms for the respective quantities
P_{arc}	Total power of the gliding arc discharge
Q_{arc}	Gliding arc heat source
r	Gliding arc radius
R_i	Net production rate of species i from combustion reactions
S	Cross-sectional area of the gliding arc
S_h	Fluid enthalpy source
$S_{i,arc}$	Net production rate of species i from plasma reactions
U	Experimentally measured voltage
V_{arc}	Gliding arc volume
x, y, z	Coordinates of a point on the ellipse after the rotation transformation
x', y', z'	Coordinates of a point on the ellipse
x_0, y_0, z_0	Center coordinates of the ellipse
Y_i	Mass fraction of species i
Y_i^*	Fine-scale species mass fraction after reacting over the timescale τ^*

their efforts to researching the GA-assisted combustion process through experimental methods. Leonov et al. [7,8] confirmed that the gas heating and high-density reactive species generated by the direct current GA can modify the flow field, achieving ignition and stable flames of H_2 and C_2H_4 at high Mach numbers. Zhang et al. [9] confirmed that gliding arc can enhance flame stability via chemical effects. Gao et al. [10] discovered that the reactive species and heat generated by the GA function as a movable pilot flame, sustaining fuel combustion. Sun et al. [11] revealed that the enhancement provided by GA discharge is not merely the result of energy deposition but rather a strong nonlinear coupling between the plasma and the turbulent flame. Feng et al. [12–14] applied the GA to the combustion chamber of a supercharged ramjet engine, discovering that the peak instantaneous power of the GA plasma is a critical factor in forming the flame core, while continuous plasma discharge contributes to the development of a larger initial flame. Besides, gliding arc can significantly enhance the flame stability of CH_4/CO_2-air mixtures and NH_3/CH_4-air mixtures [15,16]. In summary, the GA can enhance combustion stability, expand the flameout boundary of the combustion chamber, and shorten the ignition delay time. However, the physical and chemical processes underlying GA-assisted ignition are extremely complex, and experimental methods are insufficient to fully elucidate them.

Numerical models, as powerful tools for elucidating ignition and combustion mechanisms, have made significant progress in recent years in zero-dimensional plasma-assisted combustion mechanisms [17–19], various forms of plasma discharge simulations [20–23], and related areas. However, due to the strong coupling of the GA with the fluid, the challenges associated with simplifying the model to two dimensions, the complexity of plasma-assisted combustion mechanisms, large computational requirements, long discharge times, and other factors, numerical models of GA-assisted ignition pose significant challenges. Currently, research on numerical models for GA-assisted ignition is exceedingly limited. A typical simplification method of gliding arc is to consider the heat of gliding arc [24]. Wang et al. [25,26] developed a numerical model that considers the thermal effects of the GA on combustion neglecting the kinetic effects, and investigated the effects of unsteady characteristics of GA on NH_3, CH_4 ignition. Given that the GA is recognized for its strong chemical activity, further research is needed to investigate the enhancing effects of the reactive species generated by the GA.

In recent years, the development of nanosecond pulse plasma-assisted combustion models has advanced rapidly. Castela et al. [27,28] proposed a phenomenological model for nanosecond pulse plasma-assisted ignition by analyzing the channels of electrical energy deposition. The model primarily considers two energy deposition channels of the nanosecond pulse discharge: (1) rapid gas heating caused by the quenching process of excited nitrogen molecular states, leading to the dissociation of O_2 and N_2; (2) a slow gas heating process caused by vibrational excitation and relaxation reactions of nitrogen molecules. They first investigated the ignition process of methane assisted by nanosecond pulse discharge on a two-dimensional scale. Subsequently, Bechane et al. [29–31], Barléon et al. [32–34], and Malé et al. [35,36] utilized this model to study the nanosecond pulse discharge-assisted combustion process, finding that successful ignition cannot be achieved with thermal effects alone but can be achieved through combined thermal and chemical effects. Additionally, increasing the frequency of nanosecond pulse discharge can result in more uniform energy deposition, leading to faster and more stable ignition with reduced

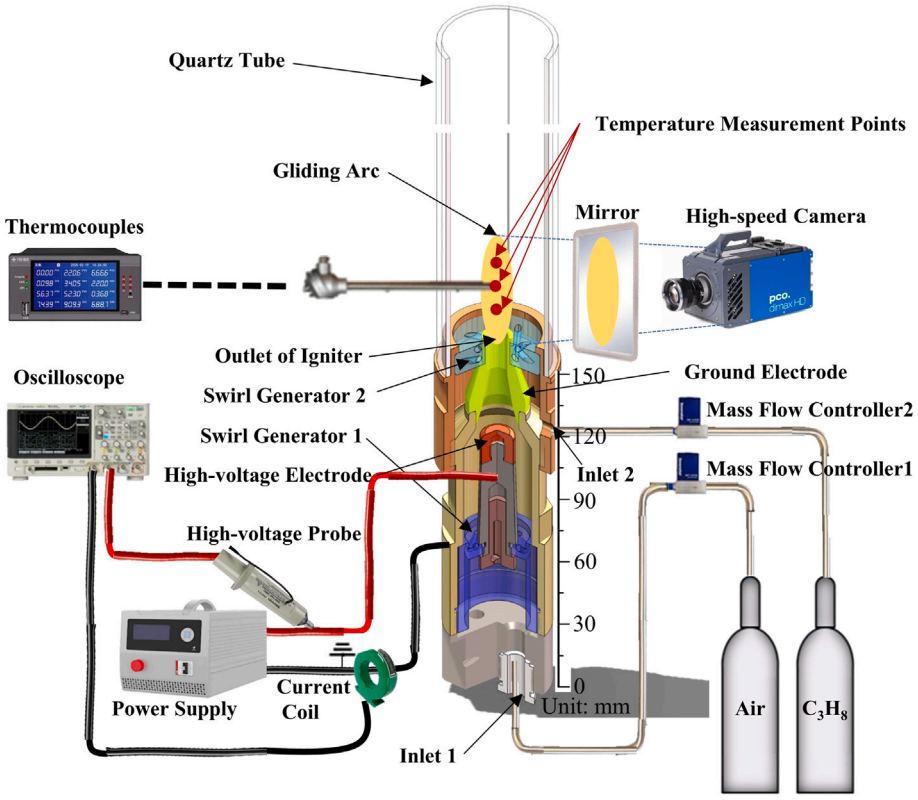

Fig. 1. Schematic of experiment and diagnosis system of swirl gliding arc igniter.

minimum required energy, while also investigating the NO_x production mechanism in the nanosecond pulse discharge-assisted ignition process. In addition to the phenomenological model, Mao et al. [23,37] proposed a two-dimensional multi-scale adaptive reduced chemistry solver for plasma assisted combustion that fully considers the energy deposition channels, and investigated the effects of non-equilibrium excitation, electrode geometry, pulse repetition frequency and pulse number on H_2/air ignition in a nanosecond pulse discharge.

In conclusion, numerical simulation studies on plasma-assisted ignition in nanosecond pulse discharge have been conducted in detail, yielding promising results. However, there is very limited numerical simulation of GA-assisted ignition, primarily due to the complex trajectory, strong coupling with flow fields, long discharge times (in milliseconds), the complexity of plasma-assisted combustion mechanisms, and other unique characteristics of the GA.

Propane serves as a critical kinetic proxy for heavier alkanes due to its position as the smallest chain molecule manifesting distinct low-temperature reactivity. A propane kinetic model including both plasma chemistry and classical combustion chemistry has been developed in our previous work [38]. So, we designate propane as the benchmark fuel for this investigation.

This work aims to simulate the GA-assisted ignition process and focus on elucidate the ignition mechanism. A new three-dimensional phenomenological gliding arc-assisted ignition model (referred to as the 3D-PM in the following text) is proposed to study the GA-assisted ignition process in detail. The structure of this paper is organized as follows: Section 2 introduces the diagnostic experiments of the swirling gliding arc igniter. Section 3 presents the 3D-PM employed in this work. Section 4 discusses the validation of simplified plasma mechanisms and simplified plasma-assisted combustion mechanisms, as well as the validation of the model with nanosecond pulse discharge and GA experiments. Section 5 studies the GA-assisted propane ignition process.

2. Gliding arc experiment setups

To validate the temperature accuracy of the 3D-PM, an experiment of the swirling gliding arc igniter was conducted, as shown in Fig. 1. Details of the experimental setup can be found in our previous work [39,40], which is designed to improve the performance of ammonia combustion assisted by GA. The experimental setup mainly consists of the gliding arc igniter, swirl generator, high-frequency high-voltage power supply (operating frequency: 23.8 kHz), gas supply system, high-speed camera, and thermocouples. The high-frequency high-voltage power supply operates at 23.8 kHz with an adjustable power range of 0 to 700 W. The swirl number of the igniter is 0.43. The detailed dimensions of igniter are shown in Fig. S17 in Supplementary Materials.

Air enters through inlet 1 and passes through swirl generator 1 to create a swirling flow field. The GA is generated between the high-voltage electrode and the ground electrode, and then moves to form a swirling GA under the influence of the swirling flow field. Inlet 2 is designed to supply propane, which passes through swirl generator 2 and comes into contact with the swirling GA to ignite it. To measure the outlet temperature of the gliding arc igniter, no propane is supplied through inlet 2. Propane is supplied through inlet 2 when capturing the propane ignition process. Two mass flow controller (Sevenstar CS200-A, 0-50 SLM and 0-5 SLM, 1.0% F.S.) regulates the airflow through inlet 1 at 30 SLM, inlet 2 at 1.2 SLM, respectively. The voltage and current of the GA discharge are measured using a high-voltage probe (Tektronix P6015 A) and a current coil (Pearson 6585), respectively, with the oscilloscope (KEYSIGHT DSOX2024 A) recording the data. A high-speed camera (PCO HS4) captures images of the GA discharge at a frame rate of 10 kHz and an exposure time of 0.089 ms. To reconstruct the trajectory of the GA, a 45° mirror is positioned at the outlet of the gliding arc igniter, allowing for capture from multiple angles. A signal generator sends trigger signals to both the oscilloscope and the high-speed camera to synchronize data recording. B-type thermocouples made of 70% platinum and 30% rhodium with 3 mm bead

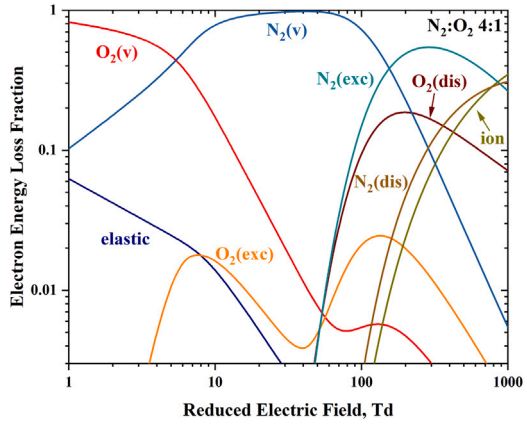

Fig. 2. Energy loss fraction of electrons deposited into different molecular degrees of freedom in air plasma from BOLSIG+.

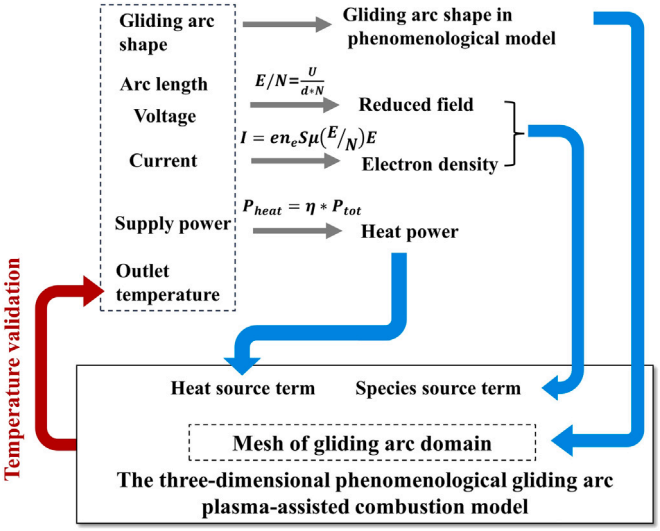

Fig. 3. Schematic of the 3D-PM.

diameter are used in the experiment, which have capable of measuring temperatures up to 1800 °C. The thermocouples are positioned at distances of 25 mm, 42 mm, and 60 mm from the igniter outlet in the GA afterglow area to measure the temperature distribution. This is because the thermocouples positioned in GA discharge area can significantly affect the GA trajectory, and the GA interferes with the proper functioning of the thermocouples. Consequently, the temperatures measured in the experiment do not reflect the GA temperature but rather the temperature of the GA afterglow area. The measured temperature represents the stabilized value achieved after a period of discharge operation, so a high response time of thermocouples is not required.

3. Modeling methods

3.1. Description of the 3D-PM

Energy deposition in plasma discharge occurs through the directed movement of electrons and ions under the influence of an electric field. Because electrons have a lighter mass compared to ions, they move at a faster velocity under the electric field, making their directed movement become the primary pathway for energy deposition in plasma. Due to the significant differences in mass, the energy exchange between electrons and the translational degrees of freedom of the molecules is slow. Thus, an electron impact can only transfer energy to the internal degrees of freedom of the molecules [3]. Different reduced electric fields (E/N) result in the generation of various excited states. Fig. 2 illustrates the EELF during air plasma discharge at reduced electric fields ranging from 1 to 1000 Td, which is calculated using BOLSIG+ according to the air plasma kinetic model [41]. When E/N is between 1 and 100 Td, electron energy is primarily utilized for vibrational excitation of O_2 and N_2. In the range of 100 to 700 Td, electron excitation and dissociation of O_2 and N_2 become the primary processes. When the reduced electric field exceeds 700 Td, electron energy is primarily utilized for the ionization of O_2 and N_2. The electronic excited states and vibrational excited states are quenched through collisions with other molecules, releasing heat that manifests as the thermal effect of plasma-assisted combustion. Electrons or electronically excited molecules collide with O_2 to form O, $O(^1D)$, and $O_2(a^1\Delta_g)$, promoting fuel oxidation and dissociation, thereby demonstrating the kinetic effect of plasma-assisted combustion.

The 3D-PM accounts for the thermal effect, kinetic effect, and transport effect of species. Considering the computational efforts arising from the transport effect induced by ionic wind, which requires solving the Poisson equation, ionization reactions, and charge transfer reactions, the computational demands of the model increase significantly. Additionally, there is a weak ionic wind in the GA discharge. Therefore, the 3D-PM does not consider the transport effect induced by ionic wind.

The 3D-PM cannot account for numerous reactions and species, necessitating the simplification of the detailed plasma-assisted propane oxidation mechanism. In this work, the model only accounts for reactions and species with strong chemical reactivity, showing the kinetic effects of GA. For combustion mechanisms, simplified mechanisms can be obtained using tools such as ChemRC [42], ANSYS Chemkin-Pro, or reported literature. For plasma mechanisms, the key species and reactions for plasma-assisted combustion can be identified through sensitivity analysis and pathway analysis using a coupled plasma and combustion chemistry solver (CPCC) [19], thereby extracting the plasma-assisted combustion skeletal mechanism. During the simplification processes, species and reactions primarily involved in heat release (such as N_2 and O_2 vibrational excitation reactions and V-T relaxation reactions) are not included in the skeletal mechanism. Instead, they are incorporated into the heat source term in the energy conservation equation to simulate their heat release process. Additionally, based on the EELF of the excluded species, the heating efficiency under different reduced electric fields is established to determine the heating power of the GA in the heat source term.

The logical schematic of the 3D-PM is illustrated in Fig. 3. Since the 3D-PM is not entirely physical self-consistent, it is necessary to determine the trajectory within the 3D-PM based on experimental data. In the experiment, the cross-section of the GA is circular, while its axis exhibits an irregular three-dimensional curve in space. Under the influence of airflow, it periodically undergoes a reignition-stretching-extinguishing-reignition cycle. In this model, the shape of the GA is simplified to a straight line plus half of an ellipse, as detailed in Section 3.4. One way to reduce computational complexity in the 3D-PM is to ignore reactions such as ionization, electron attachment, and charge transfer, as well as to avoid solving the Poisson equation. The specific reasons for this are discussed in the Supplementary Materials. Therefore, the electron density and electric field required for the species source terms must be determined through alternative methods.

In Ref. [21,43], The GA simulations indicate that the majority of the electron density and electron temperature in the GA are uniform. For the GA reignition events, the local electric field at the reignition position is higher than the average electric field over dozens of microseconds [44]. However, the short discharge time of these events results in minimal effects on the GA ignition processes. Therefore, in the 3D-PM, it is reasonable to assume that the electric field and electron density within the GA are uniform, and this assumption has

little effect on the electric field. The reduced electric field can be estimated using Eq. (1) based on the experimentally measured GA voltage and the length data captured by a high-speed camera. Given the experimentally measured GA current and the estimated reduced electric field, the electron density can be calculated using Eq. (2) [45], thereby determining the species source term of plasma reactions. The heat source terms can be calculated using the discharge power data and heating efficiency. The heat source term and species source term can be added using Fluent's User-Defined Function (UDF) technology. The combustion reactions can be modeled using Fluent's eddy dissipation concept (EDC) model. Ultimately, the 3D-PM can simulate three-dimensional gliding arc plasma-assisted combustion. By inputting the experimentally measured voltage and current, along with the shape and length of the GA captured by a high-speed camera, the 3D-PM can predict the temperature, species density, and ignition performance of the GA under these operating conditions.

$$E/N = \frac{U}{dN} \tag{1}$$

$$I = en_e S\mu(E/N)E \tag{2}$$

where U represents the experimentally measured voltage, d denotes the length of the GA, I stands for the experimental current, e represents the elementary charge, n_e signifies the electron density, S denotes the cross-sectional area of the GA, μ is the electron mobility calculated using BOLSIG+ [41], and E represents the electric field intensity.

3.2. Governing equations

The CFD modeling framework for combustion is implemented using the software ANSYS Fluent, which includes the mass, momentum, energy, and species conservation equations, as well as the thermodynamic equation of state [46]:

$$\frac{\partial \rho}{\partial t} + \nabla \cdot (\rho \vec{V}) = 0 \tag{3}$$

$$\frac{\partial (\rho \vec{V})}{\partial t} + \nabla \cdot (\rho \vec{V}\vec{V}) = -\nabla p + \nabla \cdot \tau + \rho \vec{g} \tag{4}$$

$$\frac{\partial (\rho E)}{\partial t} + \nabla \cdot (\rho \vec{V} E) = \nabla \cdot \left(k_{eff} \nabla T - \sum_{i=1}^{N_s} h_i \vec{J}_i + \tau \cdot \vec{V} - p\vec{V} \right) + S_h + Q_{arc} \tag{5}$$

$$\frac{\partial \left(\rho Y_i\right)}{\partial t} + \nabla \cdot \left(\rho \vec{V} Y_i\right) = -\nabla \cdot \vec{J}_i + R_i + S_{i,arc} \tag{6}$$

$$p = \bar{M} \sum_{i=1}^{N_s} \rho Y_i \frac{RT}{M_i} \tag{7}$$

where ρ is the density, $\vec{V}$ is the velocity vector, p is the pressure, τ is the stress tensor, $\vec{g}$ is the acceleration due to gravity, E is the total energy, k_{eff} is the effective thermal conductivity, h_i is the enthalpy of species i, J_i is the diffusion flux of species i, S_h is the fluid enthalpy source, Q_{arc} is the GA heat source, Y_i is the mass fraction of species i, R_i is the net production rate of species i from combustion reactions, and $S_{i,arc}$ is the net production rate of species i from plasma reactions.

3.3. Turbulent flow model and combustion model

The GA ignition process involves turbulent flow; therefore, the CFD model must solve equations for turbulent flow. In this study, the Transition SST model is employed to solve four transport equations [47]: turbulent kinetic energy (k), specific dissipation rate (ω), intermittency factor (γ), and the Reynolds-averaged momentum thickness Reynolds number ($\tilde{R}e_{\theta t}$) equation:

$$\frac{\partial}{\partial t}(\rho k) + \nabla \cdot (\rho k \vec{V}) = P_k - D_k + \nabla \cdot \left(\left(\mu + \sigma_k \mu_t\right) \nabla k \right) \tag{8}$$

$$\frac{\partial}{\partial t}(\rho \omega) + \nabla \cdot (\rho \omega \vec{V}) = P_\omega - D_\omega + \nabla \cdot \left(\left(\mu + \sigma_\omega \mu_t\right) \nabla \omega \right) + 2\left(1 - F_1\right) \frac{\rho \sigma_{\omega 2}}{\omega} \frac{\partial k}{\partial x_j} \frac{\partial \omega}{\partial x_j} \tag{9}$$

$$\frac{\partial (\rho \gamma)}{\partial t} + \nabla \cdot (\rho \vec{V} \gamma) = P_\gamma - \mathrm{D}_\gamma + \nabla \cdot \left[\left(\mu + \frac{\mu_t}{\sigma_\gamma} \right) \nabla \gamma \right] \tag{10}$$

$$\frac{\partial \left(\rho \tilde{R}e_{\theta t}\right)}{\partial t} + \nabla \cdot \left(\rho \vec{V} \tilde{R}e_{\theta t} \right) = P_{\theta t} + \nabla \cdot \left[\sigma_{\theta t} \left(\mu + \mu_t\right) \nabla \tilde{R}e_{\theta t} \right] \tag{11}$$

where σ_k, σ_ω, σ_γ are the inverse effective Prandtl numbers for k, ω, and γ, respectively; μ_t is the turbulent viscosity coefficient; P_k, P_ω, P_γ, and $P_{\theta t}$ are the production terms for the respective quantities; D_k, D_ω, and D_γ are the destruction terms for the respective quantities.

In the process of plasma-assisted ignition, where the timescale of chemical reactions approaches that of turbulent mixing, rapid chemical reactions may not be applicable. Therefore, detailed reaction kinetics mechanisms must be considered. The Eddy Dissipation Concept (EDC) combustion model is employed in the 3D-PM with the following equations [48]:

$$R_i = \rho \kappa \frac{Y_i^* - Y_i}{\tau^*} \tag{12}$$

$$\kappa = \frac{\xi^{*2}}{1 - \xi^{*3}} \tag{13}$$

$$\xi^* = C_\xi \left(\frac{\nu \varepsilon}{k^2} \right)^{1/4} \tag{14}$$

$$\tau^* = C_\tau \left(\frac{\nu}{\varepsilon} \right)^{1/2} \tag{15}$$

where τ^* is the integrated timescale, Y_i^* is the fine-scale species mass fraction after reacting over the timescale τ^*, ξ^* is the length scale, κ is the volume fraction of the fine scale, ν is the kinematic viscosity, and C_ξ is the length scale constant with a value of 2.1377.

3.4. The trajectory model of GA

The trajectory of the GA motion in the model is simplified from the trajectories captured in experiments, as shown in Fig. 4. The simplified trajectory consists of a straight line and half of an elliptical arc. The cross-section is circular in shape. The straight line segment is located inside the igniter, while the elliptical arc segment is outside the igniter, elongating and rotating under the influence of airflow. The governing equation is as follows:

$$x' = (a + a \cdot \cos(\theta) \cdot \sin(\omega t)) + x_0 \tag{16}$$

$$y' = (a + a \cdot \cos(\theta) \cdot \sin(\omega t)) + y_0 \tag{17}$$

$$z' = (b \cdot \sin(\theta)) + z_0 \tag{18}$$

where x_0, y_0, z_0 are the center coordinates of the ellipse; x', y', z' are the coordinates of a point on the ellipse; a and b are the lengths of the minor and major axis, respectively; θ is the angular coordinate, and ω is the GA rotational angular velocity. a and b are measured using Image-Pro Plus software from the images captured by high-speed camera.

Since the GA assumes an inclined elliptical shape after being blown out of the outlet by air, it is necessary to adjust its shape to account for the inclined angle:

$$\begin{bmatrix} x & y & z \end{bmatrix} = \begin{bmatrix} x' & y' & z' \end{bmatrix} \cdot \begin{bmatrix} \cos(\varphi) & 0 & -\sin(\varphi) \\ \sin(\varphi) & 0 & \cos(\varphi) \\ \cos(\varphi) & 0 & -\sin(\varphi) \end{bmatrix} \tag{19}$$

where: ϕ is the tilt angle of the GA, and x, y, z are the coordinates of a point on the ellipse after the rotation transformation.

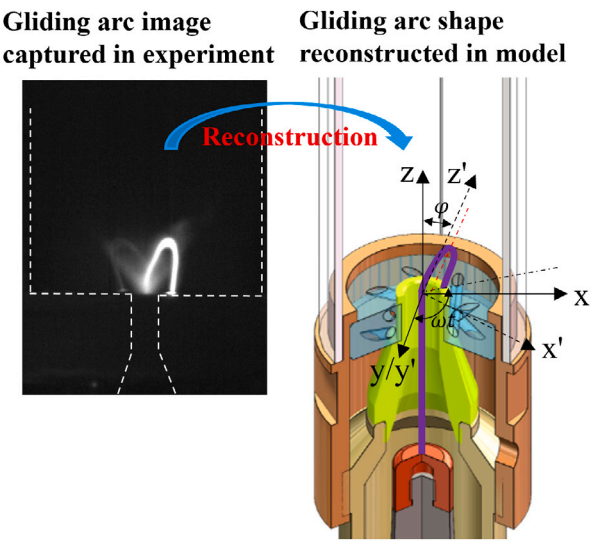

Fig. 4. Diagram of GA trajectory reconstruction in GA model.

The parameters of a, b, ϕ, and ω are obtained from the experiment. The GA root sometimes reignites or jumps randomly at an angle in a rotated direction, a behavior that is neglected in this model. The GA rotates continuously in the model with no jump events. A detailed comparison of the simplified GA trajectory and the actual GA trajectory is provided in the Supplementary Materials.

3.5. Gliding arc heat and reaction model

The GA discharge releases a significant amount of heat, directly heating the gas. Therefore, the GA heat source is incorporated into the energy equation:

$$\frac{\partial(\rho E)}{\partial t}+\nabla\cdot(\rho\vec{V}E)=\nabla\cdot\left(k_{eff}\nabla T-\sum_{i=1}^{N_s}h_i\vec{J}_i+\tau\cdot\vec{V}-p\vec{V}\right)+S_h+Q_{arc} \quad (20)$$

where: Q_{arc} is the GA heat source, which is implemented via UDF. Its expression is given by:

$$Q_{arc}=\frac{\eta P_{arc}}{V_{arc}} \quad (21)$$

$$V_{arc}=\pi r^2 L_{arc} \quad (22)$$

where: P_{arc} is the total power of the GA discharge, η is the heat efficiency of the GA, V_{arc} is the GA volume, r is the GA radius, and L_{arc} is the GA length.

The heating efficiency η is obtained as follows: as described above, a portion of the vibrationally excited state or electronically excited state is primarily quenched through relaxation reactions, releasing heat to promote combustion. Therefore, the excited species that release heat later, are neglected in the simplified mechanism, and the EELF of the electron collision processes are added up, and defined as the heating efficiency.

The heat efficiency of the mixture is obtained through the following equation:

$$\eta=\frac{\sum_i^n n_i\eta_i}{\sum_i^n n_i} \quad (23)$$

where: n_i is the mole fraction of species i, η_i is the heat efficiency of species i, and η is the heat efficiency of the mixture.

The GA discharge generates a significant amount of reactive species, promoting fuel ignition. Therefore, it is necessary to incorporate a GA discharge source into the corresponding species conservation equations:

$$\frac{\partial(\rho Y_i)}{\partial t}+\nabla\cdot(\rho J_i Y_i)=-\nabla\cdot\vec{J}_i+R_i+S_{i,arc} \quad (24)$$

$$S_{i,arc}=\sum_j^{j_{max}}k_j[A]^{\alpha}[B]^{\beta} \quad (25)$$

where α and β are the stoichiometric coefficients of species A and B, respectively, and k_j is the reaction rate coefficient.

3.6. Plasma assisted $C_3H_8/N_2/O_2$ combustion kinetic mechanism

The detailed mechanism consists of a detailed plasma sub-mechanism and a detailed combustion sub-mechanism. The detailed combustion sub-mechanism is originally from our previous work [38], which has validated with repetitively-pulsed nanosecond discharge. The detailed plasma sub-mechanism incorporates reactions of electron-impact vibrational excitation, electronic excitation, dissociation, ionization, and attachment, as well as the quenching of vibrationally and electronically excited species, charge exchange, and ion-ion and electron-ion recombination. The C_3H_8/O_2 plasma sub-mechanism is taken from our previous work [38], and the N_2 plasma sub-mechanism is obtained from Ref. [49]. The reactions of $N_2(A, a', B, C)$ with C_3H_8, C_2H_6, C_2H_4, C_2H_2, and CH_4 are obtained from Refs. [50,51].

Due to the numerous species and reactions, it is necessary to simplify the detailed plasma-assisted combustion mechanism. The reduced combustion sub-mechanism is obtained from simplified SanDiego mechanism [52]. As shown in Table 1, this work presents two reduced plasma-assisted $C_3H_8/N_2/O_2$ combustion kinetic mechanisms ("reduced1" and "reduced2"), which consist of 124 combustion reactions, 32 and 46 plasma reactions for "reduced1" and "reduced2", respectively. The detailed simplification analysis and validation of the reduced mechanisms are provided in Supplementary Materials. The two reduced mechanisms are designed to investigate the role of $O(^1D)$ in GA-assisted propane ignition. In mechanism 'reduced1', accuracy in predicting O atoms is ensured while omitting reactions related to $O_2(a^1\Delta_g)$, $O_2(b^1\Sigma_g^+)$, and $O(^1D)$ generation to prevent $O(^1D)$ production under low reduced electric fields. Conversely, it retains essential $O(^1D)$-generating reactions to preserve $O(^1D)$ production under high reduced electric fields. In mechanism 'reduced2', reactions related to $O_2(a^1\Delta_g)$, $O_2(b^1\Sigma_g^+)$, and $O(^1D)$ generation under low reduced electric fields are added based on 'reduced1' to ensure accuracy in predicting O and $O(^1D)$. Due to the low reduced electric field in GA, $N_2(A)$, $N_2(B)$, $N_2(a'1)$, and $N_2(C)$ cannot be produced effectively; therefore, the reactions between C_3H_8 and $N_2(A)$, $N_2(B)$, $N_2(a'1)$, and $N_2(C)$ are not included in Table 1.

The reduced combustion mechanism is solved throughout the entire computational domain. Reactions R1-R11 and R33-R35 from the reduced plasma mechanism are solved exclusively within the plasma discharge region, while the remaining reactions are solved globally across the entire computational domain.

3.7. The limitations of the 3D-PM

The 3D-PM accurately predicts gliding arc-assisted ignition processes and effectively captures the evolution of key species (O, $N_2(B)$, $N_2(C)$) during nanosecond pulsed discharges, along with gas temperature following V-T relaxation. Nevertheless, the limitations of the 3D-PM must be acknowledged as follows:

(a) Since the GA trajectory in the 3D-PM is derived from experimental data, the model cannot predict the performance of newly designed igniters without prior experimental data. Furthermore, it cannot assess the influence of other parameters on GA trajectory.

Table 1
The simplified plasma mechanisms used in the 3D-PM. 'reduced1' includes reactions R1-R32, and 'reduced2' includes reactions R1-R46.

Num	Reaction	Num	Reaction
R1	$e + O_2 \rightarrow e + O + O$	R17	$N_2O + N_2 \rightarrow N_2 + O + N_2$
R2	$e + O_2 \rightarrow e + O(^1D) + O$	R18	$N_2O + O_2 \rightarrow N_2 + O + O_2$
R3	$e + N_2 \rightarrow e + N_2(A)$	R19	$N_2(A) + O_2 \rightarrow N_2 + O + O(^1D)$
R4	$e + N_2 \rightarrow e + N_2(B)$	R20	$N_2(A) + O_2 \rightarrow N_2 + O + O$
R5	$e + N_2 \rightarrow e + N_2(a'1)$	R21	$N_2(A) + H_2 \rightarrow N_2 + H + H$
R6	$e + N_2 \rightarrow e + N_2(C)$	R22	$N_2(A) + H_2O \rightarrow N_2 + OH + H$
R7	$e + N_2 \rightarrow e + N + N$	R23	$N_2(B) + N_2 \rightarrow N_2(A) + N_2$
R8	$e + C_3H_8 \rightarrow e + CH_4 + C_2H_4$	R24	$N_2(B) + O_2 \rightarrow N_2 + O + O$
R9	$e + C_3H_8 \rightarrow e + CH_2 + C_2H_6$	R25	$N_2(a'1) + O_2 \rightarrow N_2 + O + O$
R10	$e + C_3H_8 \rightarrow e + CH_2 + C_2H_2 + 2H_2$	R26	$N_2(C) + O_2 \rightarrow N_2 + O + O(^1D)$
R11	$e + C_3H_8 \rightarrow e + H_2 + C_3H_6$	R27	$N_2(C) + O_2 \rightarrow N_2 + O + O$
R12	$N + O_2 \rightarrow O + NO$	R28	$O(^1D) + N_2 \rightarrow O + N_2$
R13	$N + NO \rightarrow O + N_2$	R29	$O(^1D) + O_2 \rightarrow O + O_2$
R14	$O_2 + O_2 \rightarrow O + O + O_2$	R30	$O(^1D) + C_3H_8 \rightarrow i\text{-}C_3H_7 + OH$
R15	$O_2 + O \rightarrow O + O + O$	R31	$O(^1D) + C_3H_8 \rightarrow n\text{-}C_3H_7 + OH$
R16	$N_2 + O_2 \rightarrow O + N_2O$	R32	$O(^1D) + H_2 \rightarrow OH + H$
The following reactions are unique to the 'reduced2' mechanism			
R33	$e + O_2 \rightarrow e + O_2(a^1\Delta_g)$	R40	$O_2(a^1\Delta_g) + NO \rightarrow O_2 + NO$
R34	$e + O_2 \rightarrow e + O_2(b^1\Sigma_g^+)$	R41	$O_2(a^1\Delta_g) + C_3H_8 \rightarrow O_2 + C_3H_8$
R35	$e + O \rightarrow e + O(^1D)$	R42	$O_2(b^1\Sigma_g^+) + C_3H_8 \rightarrow O_2 + C_3H_8$
R36	$O_2(b^1\Sigma_g^+) + O \rightarrow O_2 + O(^1D)$	R43	$O(^1D) + O \rightarrow O + O$
R37	$O_2(b^1\Sigma_g^+) + O_2 \rightarrow O_2(a^1\Delta_g) + O_2$	R44	$O(^1D) + O_2 \rightarrow O + O_2(b^1\Sigma_g^+)$
R38	$O_2(b^1\Sigma_g^+) + N_2 \rightarrow O_2(a^1\Delta_g) + N_2$	R45	$O + N_2 \rightarrow N + NO$
R39	$O_2(a^1\Delta_g) + O_2(a^1\Delta_g) \rightarrow O_2 + O_2(b^1\Sigma_g^+)$	R46	$O + NO \rightarrow N + O_2$

(b) The 3D-PM focuses exclusively on the spark stage without solving Poisson equation; consequently, it cannot simulate the streamer stage.
(c) The assumption of uniform electron density, which is estimated from experimental data, precludes the prediction of electron density distributions by the 3D-PM.
(d) Owing to the exclusion of ionization, electron attachment, and charge transfer reactions in the kinetic mechanism, the 3D-PM cannot predict ion density distributions.

4. Model validation

Nanosecond pulse discharge can be considered a non-equilibrium arc discharge on nanosecond scales, so validating the model with the nanosecond pulse discharge can test its predictive capacity for gas temperature and species density. Rusterholtz et al. [53] conducted repetitive nanosecond pulse discharge experiments in air and measured the temporal evolution of temperature, O, $N_2(B)$, $N_2(C)$ densities. As shown in Supplementary Materials, by validating with the experiments [53], the 3D-PM not only effectively predicts the evolution of species O, $N_2(B)$, $N_2(C)$ during nanosecond pulse discharge but also accurately forecasts gas temperature after V-T relaxation.

To validate the accuracy of the GA temperature predicted by the 3D-PM, experiments were conducted using a swirling gliding arc igniter. The experiments involved measuring the outlet temperature, shape, and voltage-current characteristics of the GA at various power levels. The detailed characteristics of the gliding arc and the selection methods of the data used in the 3D-PM are provided in Supplementary Materials.

At an airflow rate of 30 SLM and power levels ranging from 300 to 600 W, the simulation of GA in air was conducted using the "reduced1" simplified mechanism. The average temperature at the monitoring point in the model was obtained over the 60–120 ms timescale. As shown in Fig. 5, the outlet temperature increased with the rise in power levels. The radiation loss correction of thermocouples was applied in this experiment, and the emissivity of thermocouples is taken from Ref. [54]. The overall gas temperatures at different positions from the outlet in the simulation generally match the experimental measurements well. However, at low power levels, the predicted temperatures were slightly lower than the experimental temperatures, while at high power levels, they were slightly higher. This discrepancy may be attributed to the following reasons:

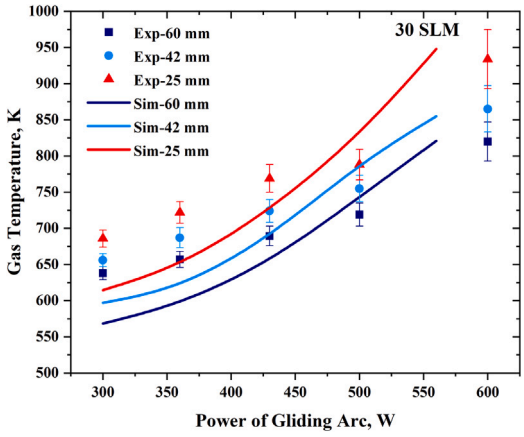

Fig. 5. The temperatures measured by thermocouples at different positions of the GA outlet at an air flow rate of 30 SLM and various power levels compared with the simulated temperatures.

(a) The model did not consider convective heat transfer with the walls, resulting in slightly higher predicted outlet temperatures at high power levels.
(b) The data selected for the input model to represent the state of the GA for this operating condition during the chosen time interval introduced some errors.
(c) The physical duration of the cases is 120 ms, while the temperature measured at the monitoring point in the experiment is recorded a few seconds after the start of the GA igniter. Therefore, the outlet temperature may not reach steady state at 120 ms at lower power levels, resulting in a slightly lower temperature predicted by the model.

In addition to the outlet temperature validation, the numerical simulation of the C_3H_8 ignition process assisted by GA is also conducted at an air flow rate of 30 SLM in inlet 1 and a C_3H_8 flow rate of 1.2 SLM in inlet 2. A description of the experiment is provided in Supplementary Materials. Fig. 6 shows the comparison of the C_3H_8 ignition process from the experiment and model. An ignition time error

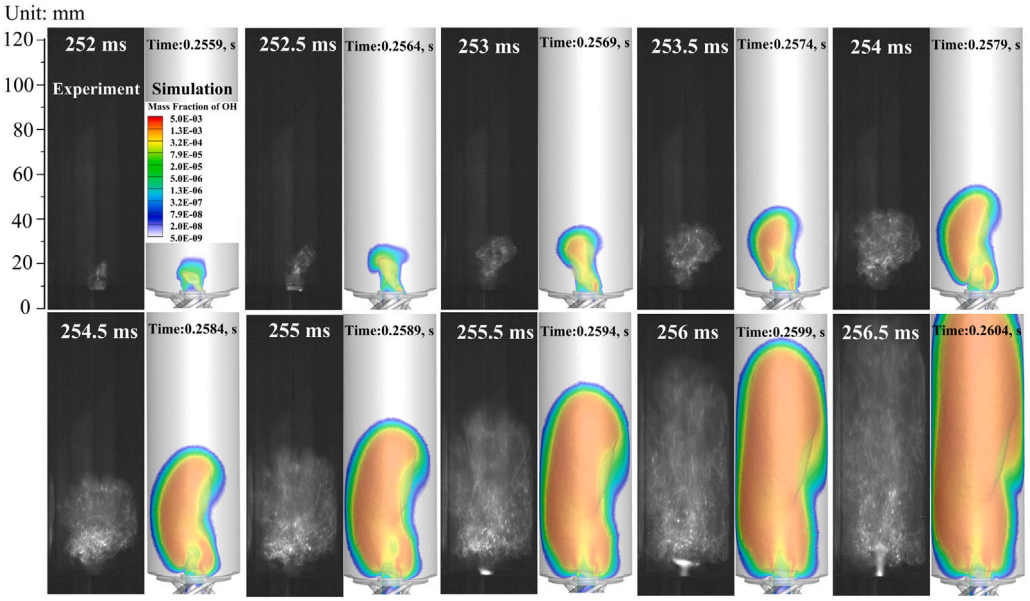

Fig. 6. The comparison of the C_3H_8 ignition process between the experiment and the model. The flame shape in model is represented by the mass fraction of OH, and the OH mass fraction of the iso-surface is 5.0×10^{-4}.

of 3.9 ms and an ignition time uncertainty of 1.6% are observed in the model compared to the experiment. This confirms that the model can accurately predict the ignition process. The complete ignition videos of the experiment and numerical simulation are also provided in Supplementary Materials.

5. Results of GA assisted propane ignition

This section employs the 3D-PM to simulate the ignition process of a propane-air mixture assisted by swirling GA plasma. The geometric configuration of the air GA ignition is illustrated in Fig. 7. The geometric configuration is simplified from the igniter structure in our previous work. [55], which is designed to improve the ignition performance of an afterburner. And it retains key structural parameters such as the swirl generator, cathode, anode, and the gap between the electrodes. Inlet 1 comprises four tangential inlets that generate a swirling flow field with a diameter of 2.6 mm and a total airflow rate of 50 SLM, corresponding to an experimental igniter inlet-outlet pressure difference of 45 Torr. Inlet 2 introduces a stoichiometric C_3H_8/air mixture at a velocity of 2 m/s, with an outlet pressure boundary condition of 1 atm. The grid independence has been conducted shown in the Supplementary Materials.

Due to the lack of self-consistency in the 3D-PM, it is necessary to incorporate experimental data (voltage, current, GA trajectory) from a single cycle of the GA in the experiment [55] into the phenomenological model. The average power of the selected GA during this time period is 1100 W, the rotational speed of the GA is 1453 rad/s, the radius of GA is 0.8 mm, and one cycle lasts 1.29 ms. As shown in Fig. 7, the GA inside the igniter is simplified to a straight line along the central axis, while the shape of the GA outside the igniter is simplified to half an ellipse, with an axial velocity of 24 m/s.

The selected GA data were incorporated into the 3D-PM, and the GA-assisted propane ignition process in air at an average power of 1100 W was simulated using the "reduced2" mechanism. The evolution of the temperature distribution is shown in Fig. 8. At 0.2 ms, there is a noticeable temperature rise within the GA channel; however, the temperature distribution is not uniform, exhibiting a "bimodal structure" along the axis, with the highest temperature near the cathode reaching approximately 4000 K. This is due to the slow gas flow near the cathode (as shown in Fig. 9), which leads to heat accumulation. Along the axis of the igniter, the temperature gradually decreases, primarily due to convective heat transfer between the swirling gas and the GA, which carries away a significant amount of heat, resulting in an overall temperature that is lower than that near the cathode. At 33 mm, the gas temperature suddenly rises. On one hand, this is because the gas at the igniter outlet is affected by centrifugal force, flowing along the outer wall, which results in reduced flow velocity near the axis of the outlet and weakened convective heat transfer, leading to a temperature increase. On the other hand, a small flame kernel forms at the outlet, with an OH mass fraction reaching 5.0×10^{-4}, as shown in Fig. 10. The combustion of propane releases heat, causing the temperature to rise.

Subsequently, from 0.4 to 1.4 ms, as shown in Figs. 8 and 10, the GA elongates while rotating, and the temperatures at both the outlet and inside the igniter gradually increase. The high-density OH region at the outlet gradually expands. At 1.4 ms, a larger flame kernel, denoted as flame kernel 1, forms at the outlet, and simultaneously, the GA reignites at this location. From 1.4 to 2.6 ms, under the influence of the airflow, flame kernel 1 moves downstream and gradually detaches from the igniter outlet. Meanwhile, the second cycle of the GA promotes the generation of a second flame kernel, flame kernel 2, which forms in close proximity to flame kernel 1. At 3.8 ms, the two flame kernels merge into a single large flame kernel. Under the continuous influence of the newly formed flame kernel at the igniter outlet, the large flame kernel develops downstream, eventually forming a large combustion region that successfully ignites the propane.

The distribution of O during the GA-assisted propane ignition process is illustrated in Fig. 11. From 0.2 to 0.4 ms, O are initially generated at the cathode, the igniter outlet, and the cathode root of the GA. However, the locations of O generation do not entirely coincide with the GA discharge channel; rather, they align closely with the distribution of gas temperature, indicating a potential association between O generation and thermal decomposition reactions. From 0.4 to 1.0 ms, with increasing temperatures, the region inside the igniter where O are produced gradually expands downstream from the vicinity of the anode-cathode. By 1.4 ms, a substantial amount of O fills the discharge channel inside the igniter. After 1.4 ms, as the GA continues to discharge, heat accumulates in the outlet region of the igniter, leading to a continuous rise in temperature. This, in turn, results in the generation of a large number of O at the cathode root of the GA and at

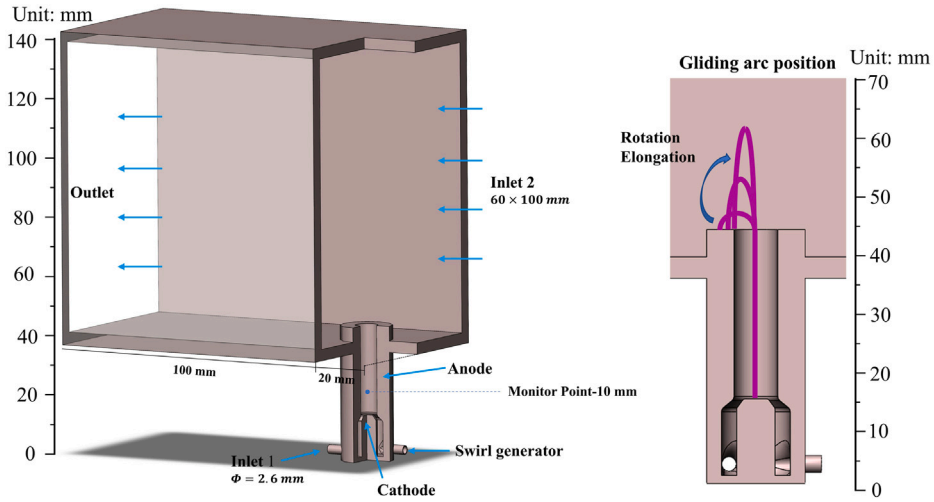

Fig. 7. Schematic of the geometric structure for GA assisted propane ignition.

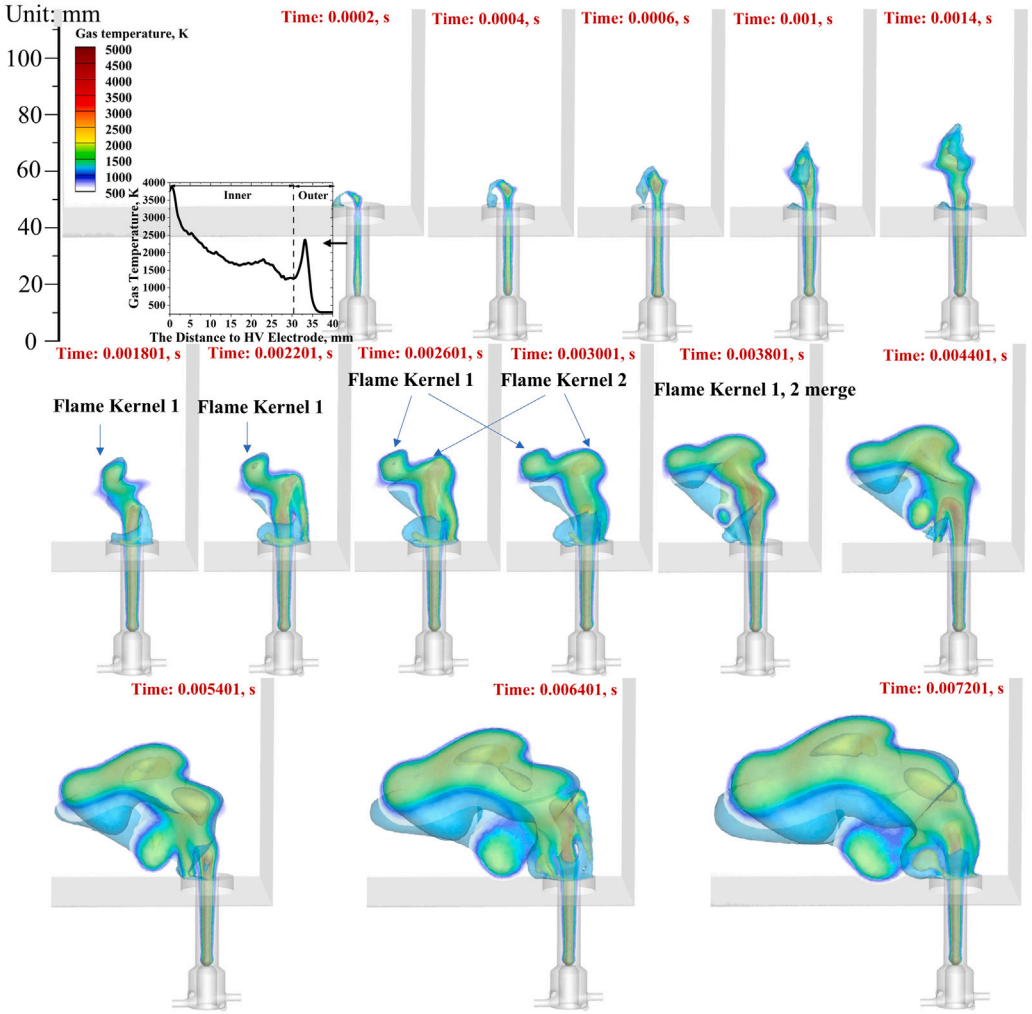

Fig. 8. Time-evolving temperature distribution for propane ignition assisted by GA in air at an average power of 1100 W. The reduced mechanism used in this model is "reduced2". The graph shows a contour map at X=0 and two gas temperature iso-surfaces, with gas temperatures of 1200 K and 2200 K.

the igniter outlet, facilitating the generation of new flame kernels and their downstream propagation.

As shown in Fig. 12, a significant amount of $O(^1D)$ is generated during the GA discharge process, primarily concentrated inside the

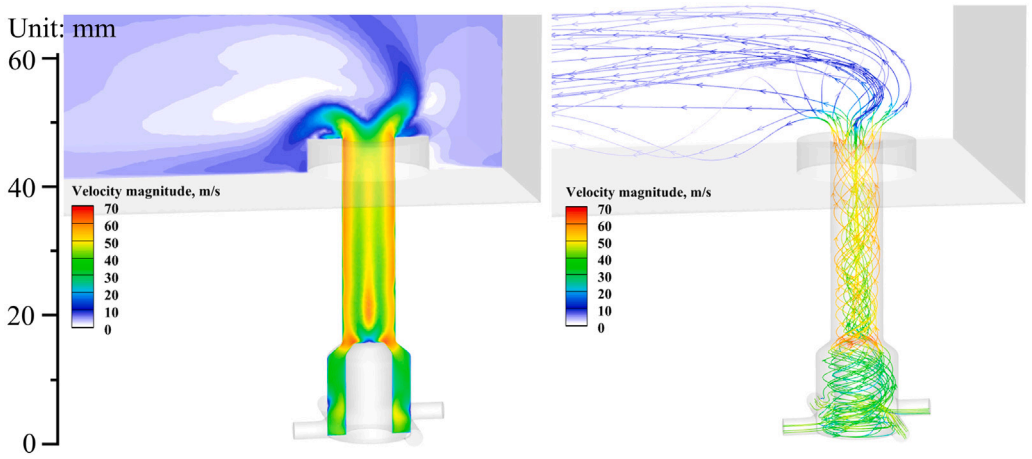

Fig. 9. Velocity flow field diagram at 0.2 ms with an average power of 1100 W.

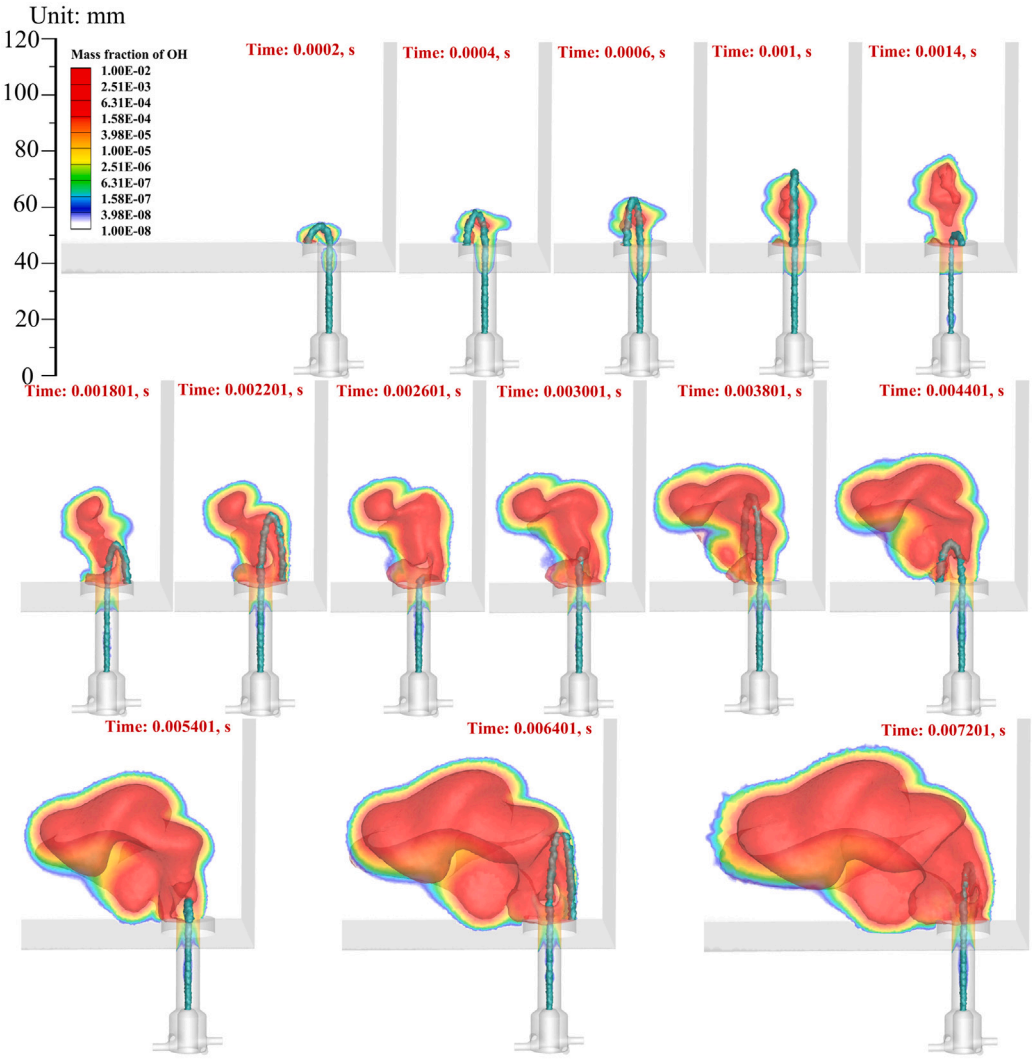

Fig. 10. The OH mass fraction distribution during GA-assisted propane ignition in air at an average power of 1100 W with an OH mass fraction of 5.0×10^{-4} on the iso-surface. The reduced mechanism used in the model is "reduced2". The dark green contour map represents iso-surfaces of electron density, used to determine the location of the GA.

igniter and at the outlet, with an $O(^1D)$ mass fraction exceeding 5.0×10^{-4}. Simultaneously, a substantial amount of $O_2(a^1\Delta_g)$ and $O_2(b^1\Sigma_g^+)$ is also produced in the GA discharge region. The mass fraction of $O_2(a^1\Delta_g)$ exceeds 5.0×10^{-4}, whereas the mass fraction of $O_2(b^1\Sigma_g^+)$ exceeds 5.0×10^{-6}, which is two orders of magnitude lower than that of $O_2(a^1\Delta_g)$. Due to the relatively low reduced electric field in the GA, $O_2(a^1\Delta_g)$ and $O_2(b^1\Sigma_g^+)$ are formed through collisions between electrons and O_2 molecules. However, the reaction $e + O_2 \rightarrow e + O + O(^1D)$ cannot

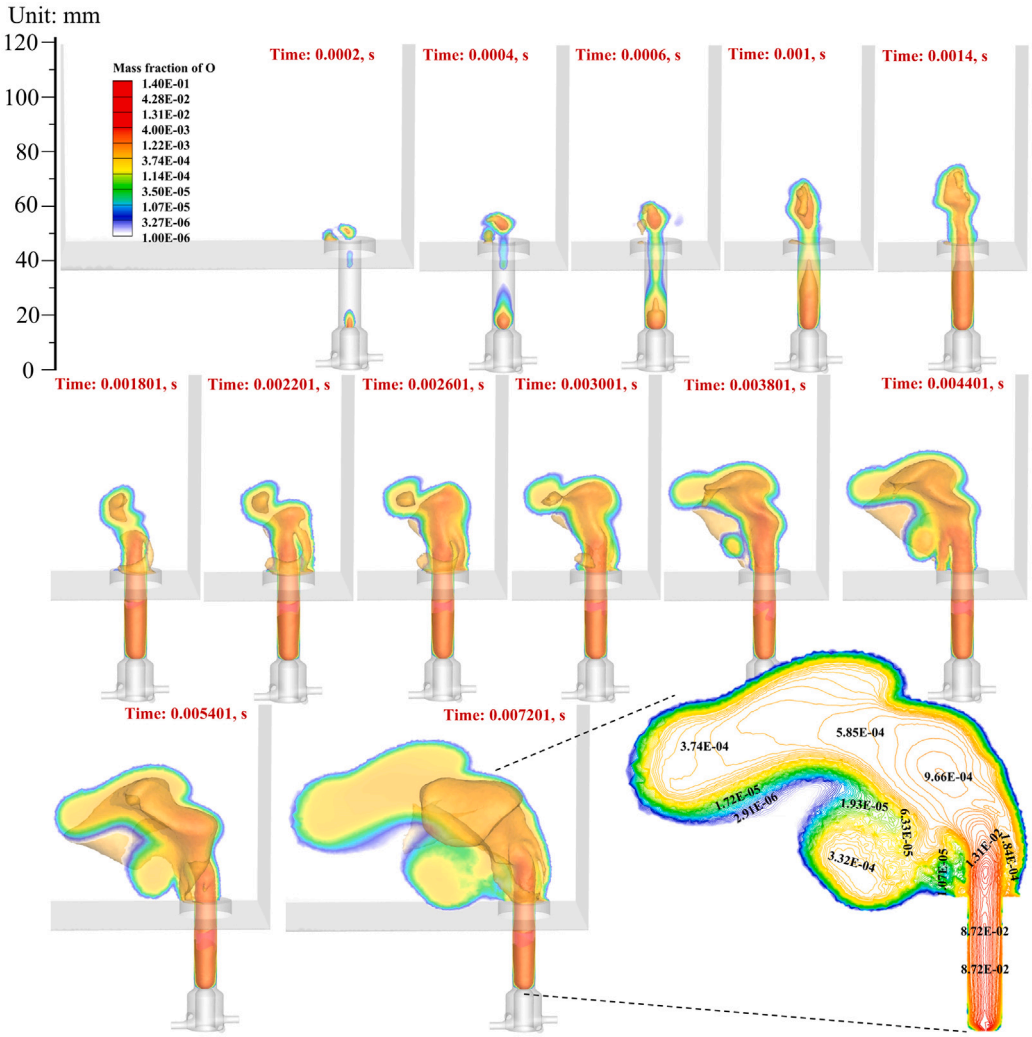

Fig. 11. The O mass fraction distribution during GA-assisted propane ignition in air at an average power of 1100 W with an O mass fraction of 5.0×10^{-4} on the iso-surface. The reduced mechanism used in the model is "reduced2". The dark green contour map represents iso-surfaces of electron density, used to determine the location of the GA.

Table 2
GA discharge data at a distance of 10 mm from the cathode under an average power of 1100 W.

Average gas temperature, K	Average reduced field, Td	Average electron density, cm^{-3}
4610	5.1	2.4×10^{14}

be the main generation pathway due to the low reaction rate in a low reduced field.

To clarify the generation pathways of $O(^1D)$, we extract the average reduced electric field, temperature, O_2 mass fraction, and average electron density at a distance of 10 mm from the cathode, as shown in Table 2. Then, these parameters are input into ZDPlasKin [56] to perform a detailed plasma kinetic simulation.

As shown in Fig. 13, $O(^1D)$ is primarily generated through collisions of electrons, $O_2(b^1\Sigma_g^+)$ with O; subsequently, $O(^1D)$ is quenched by collisions with O, maintaining the equilibrium between O and $O(^1D)$. Therefore, the key to generating $O(^1D)$ in GA with low reduced electric field discharges lies in the production of a large number of O. It is noted that 51% of O atoms are produced by the reaction $O_2 + O \rightarrow O + O + O$, and 19% of O atoms are produced through the reaction $O_2 + N \rightarrow O + NO$, both of which have reaction rate coefficients positively correlated with temperature. Thus, higher temperatures in GA discharges produce more O atoms and, consequently, more $O(^1D)$.

$O_2(a^1\Delta_g)$ and $O_2(b^1\Sigma_g^+)$ contribute to the combustion enhancement process through the heat released during their quenching. According to Fig. 13, $O_2(a^1\Delta_g)$ primarily acts to release heat in air GA, while $O_2(b^1\Sigma_g^+)$ promotes the generation of $O(^1D)$ through the reaction $O_2(b^1\Sigma_g^+) + O \rightarrow O_2 + O(^1D)$, accounting for 28% of the total $O(^1D)$ generation. Therefore, in the process of GA-assisted propane combustion at 1100 W, the role of $O_2(a^1\Delta_g)$ can be disregarded, while $O_2(b^1\Sigma_g^+)$ indirectly promotes the generation of $O(^1D)$, despite not directly aiding in C_3H_8 oxidation.

It has been confirmed that $O(^1D)$ has significant contribution to ignition in nanosecond pulse discharge [17,57,58]. However, the role of $O(^1D)$ in GA-assisted ignition is unclear. To investigate the role of $O(^1D)$, simulations were conducted using a simplified mechanism called "reduced1", which does not generate $O(^1D)$ under low reduced electric field conditions, as shown in Fig. 14. It was observed that even in the absence of $O(^1D)$, propane ignition could still occur within 7 ms, and the development of the ignition kernel was essentially consistent

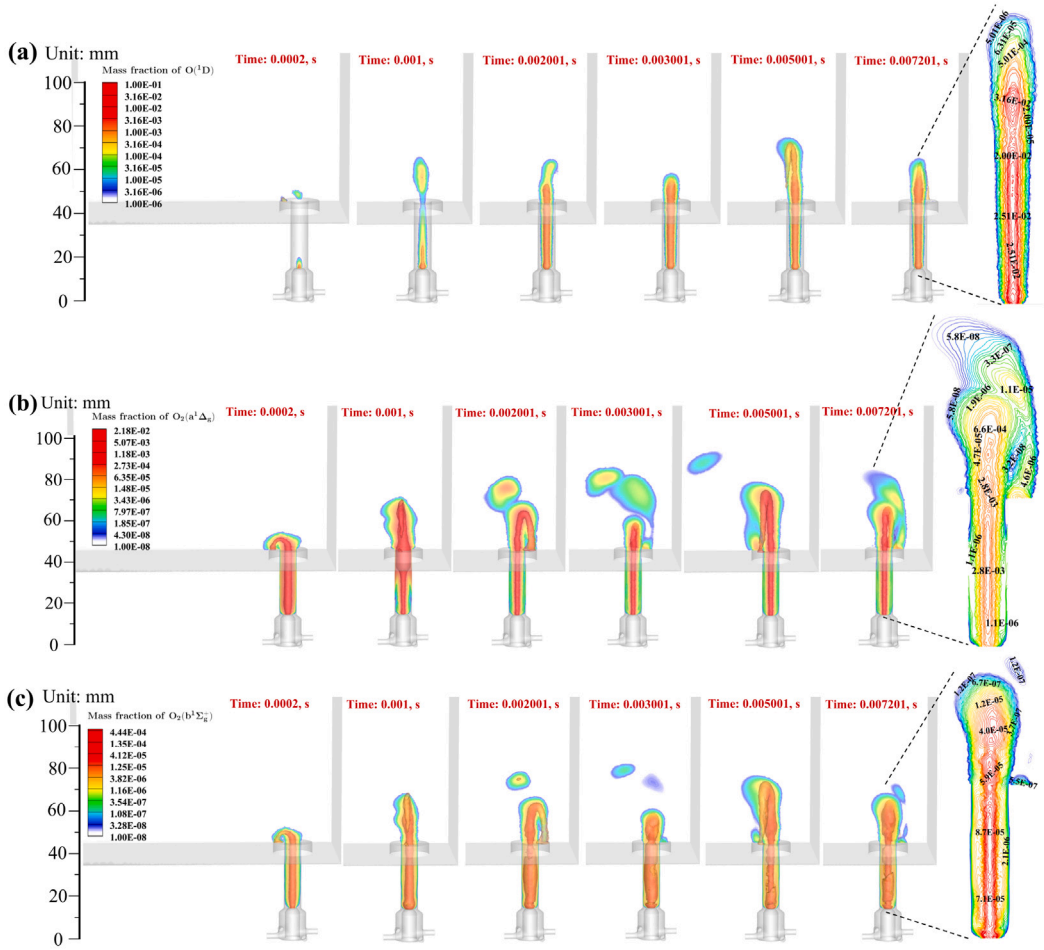

Fig. 12. The $O(^1D)$, $O_2(a^1\Delta_g)$, $O_2(b^1\Sigma_g^+)$ mass fraction distribution during GA-assisted propane ignition in air at an average power of 1100 W with the $O(^1D)$, $O_2(a^1\Delta_g)$, $O_2(b^1\Sigma_g^+)$ mass fraction of 5.0×10^{-4}, 5.0×10^{-6}, 5.0×10^{-4} on the iso-surface, respectively. The reduced mechanism used in the model is "reduced2".

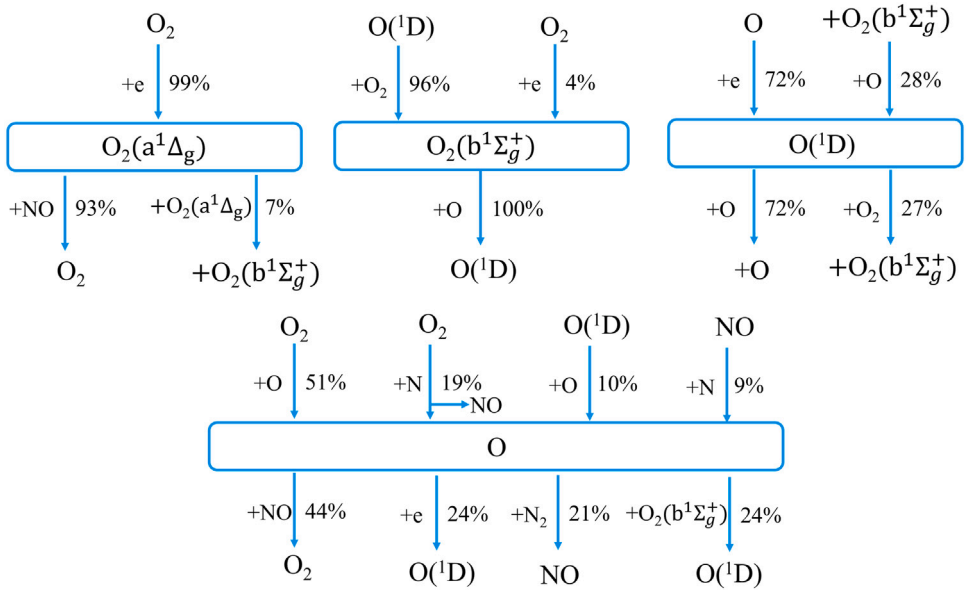

Fig. 13. At an average power of 1100 W, the generation and consumption pathways of $O_2(a^1\Delta_g)$, $O_2(b^1\Sigma_g^+)$, $O(^1D)$, and O at a distance of 10 mm from the cathode in the GA.

with the case where $O(^1D)$ was present. This suggests that at high GA discharge powers and elevated temperatures within the discharge channel, although up to 1% of $O(^1D)$ can be generated, $O(^1D)$ does not significantly impact the development of the ignition kernel in propane ignition. This observation may be attributed to the high reaction rates of combustion species at elevated temperatures, resulting in a minor

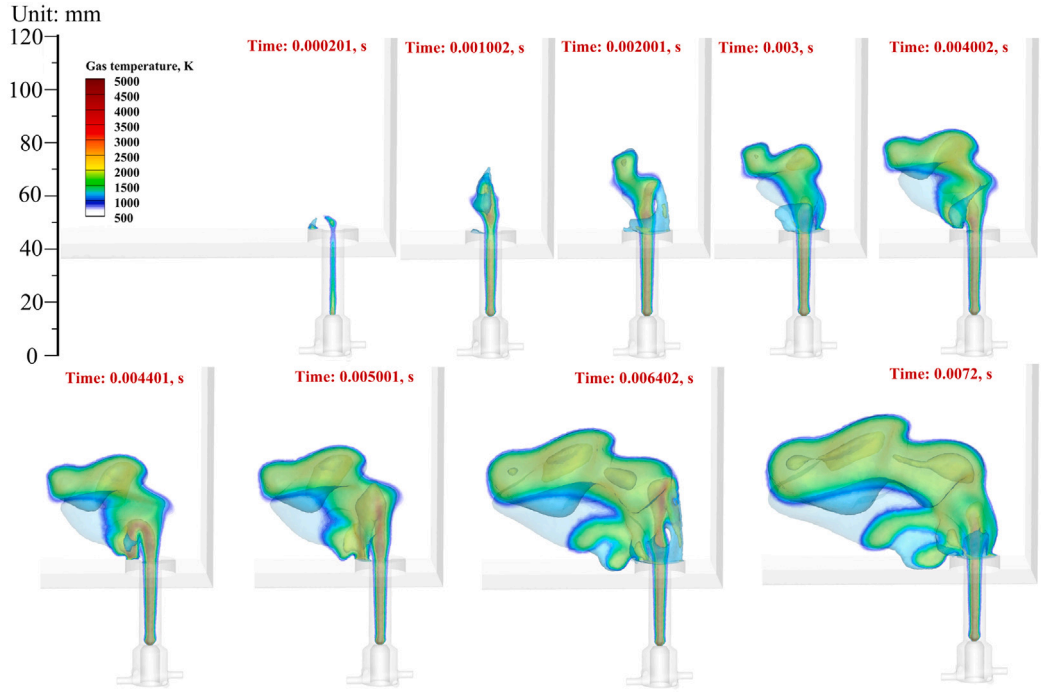

Fig. 14. Time-evolving temperature distribution for propane ignition assisted by GA in air at an average power of 1100 W. The reduced mechanism used in this model is "reduced1". The graph shows a contour map at X=0 and two gas temperature iso-surfaces, with gas temperatures of 1200 K and 2200 K.

ignition delay reduction for propane and failing to demonstrate the influence of $O(^1D)$. The new discovery resolves the knowledge gap regarding the role of $O(^1D)$ in GA-assisted combustion at high power level.

6. Conclusions

In this work, a three-dimensional phenomenological gliding arc plasma-assisted combustion model has been developed based on ANSYS Fluent. The 3D-PM considers the thermal and kinetic effects of plasma-assisted combustion processes in detail for the first time. In the thermal effect, the GA heat efficiency is determined by considering the EELF associated with vibrational degrees of freedom, as vibrational states ($N_2(v)$, $O_2(v)$) are consumed via V-T relaxation to release heat. The kinetic effect in this model is reflected in the dissociation and excitation of O_2, N_2, and C_3H_8 due to electron impact, with excited and ground states produced in the plasma discharge promoting C_3H_8 oxidation and O_2 dissociation. The GA motion trajectory is reconstructed based on experimental measurements with fairly high fidelity. The model reduces the computational complexity by ignoring reactions such as ionization, electron attachment, and charge transfer, as well as by avoiding solving the Poisson equation, the correctness of which has been confirmed by the validation against the experiment.

The detailed plasma kinetic mechanism is simplified using the sensitivity and pathway flux analysis based on CPCC. The different reduced combustion mechanisms are compared, and the best-fitting mechanism is selected based on the detailed combustion mechanism. Two reduced plasma kinetic and combustion mechanisms are proposed to investigate the role of $O(^1D)$ in GA-assisted combustion, which are well validated against the detailed mechanism in terms of ignition delay under multiple discharge conditions.

The 3D-PM is well validated against the nanosecond pulsed discharge in the evolution of O, $N_2(B)$, $N_2(C)$, and the gas temperature after V-T relaxation. Additionally, the model has been validated against outlet temperature measurements from swirling GA experiments and shows good agreement within the 300–600 W power range. And the model can simulate the GA-assisted ignition process with an ignition time uncertainty of 1.6%.

The ignition process of propane assisted by a 1100 W air GA is investigated. The temperature distribution along the axis inside the GA igniter was found to be non-uniform, exhibiting a "bimodal structure". As the GA rotates and elongates, two ignition kernels are successively formed, eventually merging to create a larger kernel that successfully ignites the propane. The GA discharge generates a significant amount of $O(^1D)$, which is firstly modeled in GA discharge. The formation and consumption of O and $O(^1D)$ in GA discharge is firstly demonstrated. O atoms are primarily produced through the thermal dissociation reactions $O_2 + O \rightarrow O + O + O$ and $O_2 + N \rightarrow O + NO$, while $O(^1D)$ is mainly generated through the reactions $O_2(b^1\Sigma_g^+) + O \rightarrow O_2 + O(^1D)$ and the electron collision reaction $e + O \rightarrow e + O(^1D)$. Thus, the production of $O(^1D)$ depends on the O generated through thermal dissociation reactions. At a power of 1100 W and a core GA temperature of 5000 K, $O(^1D)$ does not have a significant effect on the GA ignition process, which may be attributed to the high reaction rates of combustion species at elevated temperatures, that fail to demonstrate the influence of $O(^1D)$. The new discovery resolves the knowledge gap regarding the role of $O(^1D)$ in GA-assisted combustion at high power level.

CRediT authorship contribution statement

Zhenyang Li: Writing – original draft, Validation, Methodology, Formal analysis. **Ningqiu Zhao:** Validation, Investigation. **Xiaochi Ma:** Methodology, Investigation. **Bo Yin:** Methodology, Investigation. **Qifu Lin:** Writing – review & editing, Supervision. **Yifei Zhu:** Writing – review & editing, Conceptualization. **Yun Wu:** Project administration, Funding acquisition. **Yiman Jiang:** Software, Investigation.

Declaration of competing interest

The authors declare that they have no known competing financial interests or personal relationships that could have appeared to influence the work reported in this paper.

Acknowledgments

This work was supported by the National Natural Science Foundation Basic Science Center Project (No. 52488101), the National Natural Science Foundation of China (No. 52277168, 52025064, 92271113, 52207151), the National Key Research and Development Program of China (No. 2022YFC2604002, No. 2023YFB4005700, No. 2023YFB4005705, and No. 2023YFB4005702-03), the University Synergy Innovation Program of Anhui Province (No. GXXT-2022025), and the independent project of the Energy Research Institute of Hefei Comprehensive National Science Center (Anhui Energy Laboratory) (No. 22KZZ525, No. 23KZS402, No. 22KZS301, and No. 22KZS304). The authors thank the young research group in Atelier des Plasmas for fruitful discussions and the Gongfang Tech Co, Ltd for technical support. Numerical computations were performed on Hefei advanced computing center.

Appendix A. Supplementary data

Supplementary material related to this article can be found online at https://doi.org/10.1016/j.tsep.2025.103888.

Data availability

Data will be made available on request.

References

[1] L. Rosocha, D. Coates, D. Platts, S. Stange, Plasma-enhanced combustion of propane using a silent discharge, Phys. Plasmas 11 (5) (2004) 2950–2956.
[2] B. Gawron, T. Białecki, Impact of a jet A-1/HEFA blend on the performance and emission characteristics of a miniature turbojet engine, Int. J. Environ. Sci. Technol. 15 (2018) 1501–1508.
[3] A. Starikovskiy, N. Aleksandrov, Plasma-assisted ignition and combustion, Prog. Energy Combust. Sci. 39 (1) (2013) 61–110.
[4] Y. Ju, W. Sun, Plasma assisted combustion: Dynamics and chemistry, Prog. Energy Combust. Sci. 48 (2015) 21–83.
[5] M. Li, Z. Wang, R. Xu, X. Zhang, Z. Chen, Q. Wang, Advances in plasma-assisted ignition and combustion for combustors of aerospace engines, Aerosp. Sci. Technol. 117 (2021) 106952.
[6] A. Fridman, Plasma Chemistry, Cambridge University Press, 2008.
[7] S. Leonov, D. Yarantsev, C. Carter, Experiments on electrically controlled flameholding on a plane wall in a supersonic airflow, J. Propuls. Power 25 (2) (2009) 289–294.
[8] S.B. Leonov, I.V. Kochetov, A.P. Napartovich, V.A. Sabel'Nikov, D.A. Yarantsev, Plasma-induced ethylene ignition and flameholding in confined supersonic air flow at low temperatures, IEEE Trans. Plasma Sci. 39 (2) (2010) 781–787.
[9] Y. Zhang, T. Li, X. Wei, Influence of non-thermal plasma and electric field on non-premixed methane flame, Therm. Sci. Eng. Prog. 47 (2024) 102366.
[10] J. Gao, C. Kong, J. Zhu, A. Ehn, T. Hurtig, Y. Tang, S. Chen, M. Aldén, Z. Li, Visualization of instantaneous structure and dynamics of large-scale turbulent flames stabilized by a gliding arc discharge, Proc. Combust. Inst. 37 (4) (2019) 5629–5636.
[11] J. Sun, Y. Tang, S. Li, Plasma-assisted stabilization of premixed swirl flames by gliding arc discharges, Proc. Combust. Inst. 38 (4) (2021) 6733–6741.
[12] R. Feng, Y. Huang, J. Zhu, Z. Wang, M. Sun, H. Wang, Z. Cai, Ignition and combustion enhancement in a cavity-based supersonic combustor by a multi-channel gliding arc plasma, Exp. Therm. Fluid Sci. 120 (2021) 110248.
[13] R. Feng, Z. Wang, M. Sun, H. Wang, Y. Huang, Y. Yang, X. Liu, C. Wang, Y. Tian, T. Luo, et al., Multi-channel gliding arc plasma-assisted ignition in a kerosene-fueled model scramjet engine, Aerosp. Sci. Technol. 126 (2022) 107606.
[14] R. Feng, J. Zhu, Z. Wang, F. Zhang, Y. Ban, G. Zhao, Y. Tian, C. Wang, H. Wang, Z. Cai, et al., Suppression of combustion mode transitions in a hydrogen-fueled scramjet combustor by a multi-channel gliding arc plasma, Combust. Flame 237 (2022) 111843.
[15] A. Ghabi, T. Darny, S. Dozias, P.E. Bocanegra, J.-M. Pouvesle, B. Sarh, E. Robert, T. Boushaki, Effects of pulsed gliding arc plasma on non-premixed CH4/CO2–air flame stability, Therm. Sci. Eng. Prog. 40 (2023) 101764.
[16] A. Jančauskas, R. Paulauskas, E. Bykov, K. Zakarauskas, I. Ambrazevičius, Gliding arc plasma effect on thermal characteristics of ammonia/biogas flames, Therm. Sci. Eng. Prog. (2025) 103494.
[17] X. Mao, A. Rousso, Q. Chen, Y. Ju, Numerical modeling of ignition enhancement of CH4/O2/He mixtures using a hybrid repetitive nanosecond and DC discharge, Proc. Combust. Inst. 37 (4) (2019) 5545–5552.
[18] N. Tsolas, R.A. Yetter, I.V. Adamovich, Kinetics of plasma assisted pyrolysis and oxidation of ethylene. Part 2: Kinetic modeling studies, Combust. Flame 176 (2017) 462–478.
[19] Y. Qiu, Y. Zhu, Y. Wu, N. Zhao, Z. Li, M. Hao, B. Zhang, D. Pan, Numerical investigation of the hybrid pulse–DC plasma assisted ignition and NOx emission of NH3/N2/O2 mixture, Combust. Flame 258 (2023) 113078.
[20] K. Mazaheri, J. Omidi, K. Kiani, Simulation of DBD plasma actuator effect on aerodynamic performance improvement using a modified phenomenological model, Comput. & Fluids 140 (2016) 371–384.
[21] S. Kolev, A. Bogaerts, A 2D model for a gliding arc discharge, Plasma Sources Sci. Technol. 24 (1) (2014) 015025.
[22] S. Van Alphen, J. Slaets, S. Ceulemans, M. Aghaei, R. Snyders, A. Bogaerts, Effect of N2 on CO2-CH4 conversion in a gliding arc plasmatron: Can this major component in industrial emissions improve the energy efficiency? J. CO2 Util. 54 (2021) 101767.
[23] X. Mao, H. Zhong, T. Zhang, A. Starikovskiy, Y. Ju, Modeling of the effects of non-equilibrium excitation and electrode geometry on H2/air ignition in a nanosecond plasma discharge, Combust. Flame 240 (2022) 112046.
[24] D. Sharma, A. Mistry, H. Mistry, P. Chaudhuri, P. Murugan, S. Patnaik, A. Sanghariyat, V. Jain, S. Chaturvedi, S. Nema, Thermal performance analysis and experimental validation of primary chamber of plasma pyrolysis system during preheating stage using CFD analysis in ANSYS CFX, Therm. Sci. Eng. Prog. 18 (2020) 100525.
[25] Y. Wang, C. Kong, X. Wu, Z. Zhang, Characteristics of rotating gliding arc induced thermal ignition of lean methane-air mixtures, Appl. Energy Combust. Sci. 14 (2023) 100154.
[26] Y. Wang, C. Kong, C. Wang, X. Wu, Z. Zhang, Characteristics of unsteady rotating gliding arc induced ignition of ammonia–air mixture in swirling flow, Fuel 364 (2024) 131117.
[27] M. Castela, B. Fiorina, A. Coussement, O. Gicquel, N. Darabiha, C.O. Laux, Modelling the impact of non-equilibrium discharges on reactive mixtures for simulations of plasma-assisted ignition in turbulent flows, Combust. Flame 166 (2016) 133–147.
[28] M. Castela, S. Stepanyan, B. Fiorina, A. Coussement, O. Gicquel, N. Darabiha, C.O. Laux, A 3-D DNS and experimental study of the effect of the recirculating flow pattern inside a reactive kernel produced by nanosecond plasma discharges in a methane-air mixture, Proc. Combust. Inst. 36 (3) (2017) 4095–4103.
[29] Y. Bechane, B. Fiorina, Numerical investigations of turbulent premixed flame ignition by a series of nanosecond repetitively pulsed discharges, Proc. Combust. Inst. 38 (4) (2021) 6575–6582.
[30] Y. Bechane, B. Fiorina, Numerical analysis of turbulent flame enhancement by nanosecond repetitively pulsed plasma discharges, Proc. Combust. Inst. 39 (4) (2023) 5465–5476.
[31] Y. Bechane, B. Fiorina, A numerical investigation of plasma-assisted ignition by a burst of nanosecond repetitively pulsed discharges, Combust. Flame 259 (2024) 113106.
[32] N. Barléon, B. Cuenot, O. Vermorel, Large-eddy simulation of swirled flame stabilisation using NRP discharges at atmospheric pressure, Appl. Energy Combust. Sci. 15 (2023) 100163.
[33] N. Barleon, L. Cheng, B. Cuenot, O. Vermorel, A. Bourdon, Investigation of the impact of NRP discharge frequency on the ignition of a lean methane-air mixture using fully coupled plasma-combustion numerical simulations, Proc. Combust. Inst. 39 (4) (2023) 5521–5530.
[34] N. Barléon, L. Cheng, B. Cuenot, O. Vermorel, A phenomenological model for plasma-assisted combustion with NRP discharges in methane-air mixtures: PACMIND, Combust. Flame 253 (2023) 112794.
[35] Q. Malé, S. Shcherbanev, N. Noiray, Numerical study of plasma assisted combustion in a sequential combustor, Proc. Combust. Inst. 39 (4) (2023) 5447–5456.
[36] Q. Malé, N. Barléon, S. Shcherbanev, B. Dharmaputra, N. Noiray, Numerical study of nitrogen oxides chemistry during plasma assisted combustion in a sequential combustor, Combust. Flame 260 (2024) 113206.
[37] X. Mao, H. Zhong, Z. Wang, T. Ombrello, Y. Ju, Effects of inter-pulse coupling on nanosecond pulsed high frequency discharge ignition in a flowing mixture, Proc. Combust. Inst. 39 (4) (2023) 5457–5464.
[38] Z. Li, B. Yin, Q. Lin, Y. Zhu, Y. Wu, Kinetic development of low-temperature propane oxidation in a repetitively-pulsed nanosecond discharge, Combust. Flame 274 (2025) 114023.
[39] Q. Lin, Y. Jiang, C. Liu, L. Chen, W. Zhang, J. Ding, J. Li, Instantaneous hydrogen production from ammonia by non-thermal arc plasma combining with catalyst, Energy Rep. 7 (2021) 4064–4070.
[40] Q. Lin, Y. Jiang, C. Liu, L. Chen, W. Zhang, J. Ding, J. Li, Controllable NO emission and high flame performance of ammonia combustion assisted by non-equilibrium plasma, Fuel 319 (2022) 123818.
[41] G. Hagelaar, L.C. Pitchford, Solving the Boltzmann equation to obtain electron transport coefficients and rate coefficients for fluid models, Plasma Sources Sci. Technol. 14 (4) (2005) 722.
[42] W. Sun, Z. Chen, X. Gou, Y. Ju, A path flux analysis method for the reduction of detailed chemical kinetic mechanisms, Combust. Flame 157 (7) (2010) 1298–1307.

[43] S. Sun, S. Kolev, H. Wang, A. Bogaerts, Coupled gas flow-plasma model for a gliding arc: investigations of the back-breakdown phenomenon and its effect on the gliding arc characteristics, Plasma Sources Sci. Technol. 26 (1) (2016) 015003.
[44] J. Zhu, J. Gao, A. Ehn, M. Aldén, A. Larsson, Y. Kusano, Z. Li, Spatiotemporally resolved characteristics of a gliding arc discharge in a turbulent air flow at atmospheric pressure, Phys. Plasmas 24 (1) (2017) 013514.
[45] N. Popov, Fast gas heating initiated by pulsed nanosecond discharge in atmospheric pressure air, in: 51st AIAA Aerospace Sciences Meeting Including the New Horizons Forum and Aerospace Exposition, 2013, p. 1052.
[46] S. Yuze, C. Tao, M. Shahsavari, S. Dakun, S. Xiaofeng, Z. Dan, W. Bing, RANS simulations on combustion and emission characteristics of a premixed NH3/H2 swirling flame with reduced chemical kinetic model, Chin. J. Aeronaut. 34 (12) (2021) 17–27.
[47] U. Divakaran, A. Ramesh, A. Mohammad, R.K. Velamati, Effect of helix angle on the performance of helical vertical axis wind turbine, Energies 14 (2) (2021) 393.
[48] Ansys fluent theory guide, 2021, Release 2021.
[49] Y. Zhu, N.D. Lepikhin, I.S. Orel, A. Salmon, A.V. Klochko, S.M. Starikovskaia, Optical actinometry of O-atoms in pulsed nanosecond capillary discharge: peculiarities of kinetics at high specific deposited energy, Plasma Sources Sci. Technol. 27 (7) (2018) 075020.
[50] N. Moreau, S. Pasquiers, N. Blin-Simiand, L. Magne, F. Jorand, C. Postel, J. Vacher, Propane dissociation in a non-thermal high-pressure nitrogen plasma, J. Phys. D: Appl. Phys. 43 (28) (2010) 285201.
[51] A. Starikovskiy, Mechanism of plasma-assisted ignition for H2 and C1-C5 hydrocarbons, in: 55th AIAA Aerospace Sciences Meeting, 2017, p. 1977.
[52] K.C. Lin, C.-T. Chiu, A compact skeletal mechanism of propane towards applications from NTC-affected ignition predictions to CFD-modeled diffusion flames: Comparisons with experiments, Fuel 203 (2017) 102–112.
[53] D.L. Rusterholtz, D.A. Lacoste, G.D. Stancu, D.Z. Pai, C.O. Laux, Ultrafast heating and oxygen dissociation in atmospheric pressure air by nanosecond repetitively pulsed discharges, J. Phys. D: Appl. Phys. 46 (46) (2013) 464010.
[54] V. Hindasageri, R. Vedula, S. Prabhu, Thermocouple error correction for measuring the flame temperature with determination of emissivity and heat transfer coefficient, Rev. Sci. Instrum. 84 (2) (2013) 024902.
[55] X. Cheng, S. Huimin, S. Huang, Z. Yifei, Z. Zhang, L. Zhenyang, J. Min, Discharge and jet characteristics of gliding arc plasma igniter driven by pressure difference, Plasma Sci. Technol. 24 (11) (2022) 115502.
[56] S. Pancheshnyi, B. Eismann, G. Hagelaar, L. Pitchford, Computer Code ZD PlasKin, University of Toulouse, Toulouse, France, 2008, Laplace, CNRS-UPS-INP. URL: http://www.zdplaskin.laplace.univ-tlse.fr.
[57] J.K. Lefkowitz, P. Guo, A. Rousso, Y. Ju, Species and temperature measurements of methane oxidation in a nanosecond repetitively pulsed discharge, Philos. Trans. R. Soc. A: Math. Phys. Eng. Sci. 373 (2048) (2015) 20140333.
[58] S. Yang, X. Gao, V. Yang, W. Sun, S. Nagaraja, J.K. Lefkowitz, Y. Ju, Nanosecond pulsed plasma activated C2h4/O2/Ar mixtures in a flow reactor, J. Propuls. Power 32 (5) (2016) 1240–1252.